Physics-Based, Neural Network Force Fields for Reactive Molecular Dynamics: Investigation of Carbene Formation from [EMIM$^+$][OAc$^-$]

John P. Stoppelman[1] and Jesse G. McDaniel[1]

School of Chemistry and Biochemistry, Georgia Institute of Technology

Atlanta, Georgia, 30332-0400, United States

(*Electronic mail: mcdaniel@gatech.edu)

(Dated: 18 August 2021)

Reactive molecular dynamics simulations enable detailed understanding of solvent effects on chemical reaction mechanisms and reaction rates. While classical molecular dynamics using reactive force fields allows significantly longer simulation time scales and larger system sizes compared with *ab initio* molecular dynamics, constructing reactive force fields is a difficult and complex task. In this work, we describe a general approach following the Empirical Valence Bond (EVB) framework for constructing *ab initio* reactive force fields for condensed phase simulations by combining physics-based methods with neural networks (PB/NN). The physics-based terms ensure correct asymptotic behavior of electrostatic, polarization, and dispersion interactions, and are compatible with existing solvent force fields. Neural networks are utilized for versatile description of short-range orbital interactions within the transition state region, and accurate rendering of vibrational motion of the reacting complex. We demonstrate our methodology for a simple deprotonation reaction of the 1-ethyl-3-methylimidazolium (EMIM$^+$) cation with acetate to form 1-ethyl-3-methylimidazol-2-ylidene and acetic acid. Our PB/NN force field exhibits ~ 1 kJ mol^{-1} MAE accuracy within the transition state region for the gas-phase complex. To characterize solvent modulation of the reaction profile, we compute potentials of mean force (PMFs) for the gas-phase reaction as well as the reaction within a four ion cluster, and benchmark against *ab initio* molecular dynamics simulations. We find that the surrounding ionic environment significantly destabilizes formation of the carbene product, and we show that this effect is accurately captured by the reactive force field. By construction, the PB/NN potential may be directly employed for simulations of other solvents/chemical environments without additional parameterization.

I. INTRODUCTION

Solvent effects on chemical reactions are ubiquitous in chemistry and biology, and are an important consideration when optimizing catalytic processes. The solvent may modulate the kinetics, mechanism, and/or the selectivity of a reaction, and unraveling such effects can be difficult, particularly in the presence of other catalytic species. Computational methods are useful in this regard, and approaches that involve a quantum mechanical (QM) treatment of the reacting species with implicit or continuum description of the solvent have become increasingly refined.[1,2] However, going beyond such a continuum description to a full atomistic representation of the solvent generally requires molecular dynamics (MD) simulations. MD simulations have provided significant insight into a variety of biological and chemical processes, and can, in principle, provide similar insights into the mechanisms associated with solution phase reactions.[3–8] However, MD simulations typically rely on classical force fields to describe the potential energy of the system, and these force fields generally do not describe bond-breaking/bond-forming processes, preventing their use for studying reactions. Quantum mechanical (QM) simulation methods, such as *ab initio* molecular dynamics (AIMD) or quantum mechanical/molecular mechanics (QM/MM), explicitly treat the electronic degrees of freedom involved in a reaction, but are computationally costly and are limited to small time scales and/or system sizes.[9,10] Furthermore, statistical sampling of the reaction coordinate and solvation environment is limited with these QM approaches, which may preclude their application to certain problems of interest.

Reactive force fields can potentially be used to simulate reactions in solution at a greatly reduced computational cost compared to either AIMD or QM/MM methods. A variety of such force fields exist including ReaxFF, COMB, REBO and others,[11–15] often utilizing the concept of bond-order to describe bond-breaking/forming. These force fields are designed with the goal of developing general parameters that allow for study and discovery of reactions in a variety of environments. Parameterization of such reactive force fields is intrinsically complex, however, due to the fact that transition states cannot be expressed as low-order expansions of either the reactant or product molecular properties. This is in contrast to standard (non-reactive) force fields, that make extensive use of harmonic approximations and expansions of molecular properties (charges, polarizabilities, etc.) to model intermolecular interactions. The consequence is that reactive force fields often utilize complex functional forms requiring numerous parameters, making parameter fitting/optimization difficult. Additionally, system-specific functions may be required, inhibiting

the development of a general framework for modeling chemical reactions.[16] Achieving the desired level of accuracy/stability for these types of force fields is an ongoing challenge.[17,18]

The empirical valence bond (EVB) method, originally developed by Warshel,[19,20] represents another force field approach capable of simulating reactions within condensed phase environments. In contrast to previously discussed approaches, EVB Hamiltonians are typically parameterized on a reaction-specific basis, requiring new parameterization for each different reaction of interest. The intent is thus primarily to investigate solvent effects on a particular target reaction, and not to explore or discover new or unknown chemical reactions. Within the EVB approach, a Hamiltonian is constructed with diagonal elements that represent the reactant/product/intermediate states, and off-diagonal coupling elements mediate transitions between these states. The diagonal terms typically employ standard functional forms and may consist entirely of existing force fields, while the off-diagonal elements are system-specific and generally fit to reproduce the gas-phase potential energy surface. A common ansatz of the EVB approach is that solvent effects are included purely within the diagonal elements of the Hamiltonian; within this ansatz, an EVB Hamiltonian may thus be used to study a particular reaction within different chemical environments.[19,21,22] Note, however, that other approaches incorporate solvent degrees of freedom in the off-diagonal elements as well.[23] EVB and similar approaches have been used to investigate a variety of applications, such as enzyme catalysis,[24,25] proton transport in water,[26–29] and various other solution-phase reactions.[19,30–33] A particular difficulty is that there is no consensus for the functional form of the off-diagonal elements; previous work has employed constants, exponentials, distributed Gaussians and spline fits.[19,20,28,34,35] Parameterization of EVB models to *ab initio* potential energy surfaces would require sufficiently versatile functional forms for the off-diagonal elements in order to generally achieve chemical accuracy within the transition state region.

Recent advances in machine learning and neural network parameterization offer new avenues for progress in reactive force field development. Particularly, these methods provide a general and versatile framework for accurately rendering "difficult-to-capture" regions of high dimensional, potential energy surfaces. Artificial neural networks (NNs) are universal function approximators, with demonstrated ability to accurately model chemical bond-breaking and forming processes.[36] Various neural network architectures have successfully reproduced reaction potential energy surfaces, such as PhysNet, DeepPot and others.[37–39] However, there are some key limitations associated with using neural network potentials to simulate reactions in solution. Most commonly, neural network potentials use a sum of atomic energies to represent the total energy of the system, gen-

erated from a set of descriptors that encode the atomic environment.[40] Descriptors are computed with a distance-based cutoff,[40] which may prevent encoding of the correct long-range physics, particularly for electrostatic interactions. Indeed short-range truncations in both physics-based potentials,[41–43] as well as in machine learning contexts,[44] have been shown to cause unphysical artifacts in MD simulations. A related issue is the limited extrapolation capability of NNs, with unreliable predictions outside of the scope of the training data.[36]. A promising solution is to restrict the required range of the neural network by supplementing with physics-based terms, such as explicit Coulombic interactions.[37] Parameters for the physics-based terms can either be developed from direct quantum chemical calculations, or may themselves be predicted with machine learning techniques.[45,46] Further considerations for NN potentials include the large amount of training data required for parameterization, as well as simulation speed; while orders of magnitude faster than QM calculations, NNs are still generally an order of magnitude slower than the empirical reactive force fields mentioned previously.[14]

In this work, we demonstrate a general method for developing *ab initio*, reactive force fields by combining both physics-based and neural network terms within an EVB framework. The reaction that we consider is N-heterocyclic carbene (NHC) formation from 1-ethyl-3-methylimidazolium ($EMIM^+$) cation and acetate (OAc^-) anion; these ions constitute the [$EMIM^+$][OAc^-] ionic liquid (IL). In this reaction, $EMIM^+$undergoes deprotonation by acetate to form 1-ethyl-3-methylimidazol-2-ylidene (NHC) and acetic acid (AcOH):

$$EMIM^+ + OAc^- \rightleftharpoons NHC + AcOH \tag{1}$$

NHCs are highly reactive catalysts and rank among the most important tools in organocatalysis.[47,48] Imidazolium-based ionic liquids are commonly used solvents in organic chemistry due to their low vapor pressure and thermal/chemical stability;[49] because of the acidic proton of the imidazolium ring, there has been interest in using these ILs as both reagents and solvents.[50] A strong base or electrochemical reduction is often used to carry out the deprotonation of the imidazolium ring.[51,52] However, recent experimental work has suggested spontaneous NHC formation in ILs such as [$EMIM^+$][OAc^-] due to deprotonation of the imidazolium ring by weak base counterions.[50,53–55] While the formation of neutral species from two ions would seem unfavorable in ionic media, several NHC-catalyzed reactions have been shown to occur in imidazolium acetate ILs such as benzoin condensation, which may suggest carbene presence;[56–58] however, it has been pointed out there are alternative reaction pathways for formation of these products that do not involve direct

carbene formation.[54] NHC content in these ILs has been characterized with cyclic voltammetry, yet interpretation of these results is somewhat inconclusive as the electrode can act as a carbene trap.[54,59–61] Due to the short lifetimes of any produced NHCs, it is difficult to devise experiments that directly measure carbene formation in ILs.

Understanding NHC formation within imidazolium-based ionic liquids is important for a variety of applications due to the innate reactivity of carbene species. As ILs are continually used as electrolytes in energy-storage devices, it is important to know the extent to which the liquid is chemically stable.[62] Presumably, more native NHC content would lead to reduced chemical stability due to facile degradation pathways catalyzed by carbene intermediates. This could be either beneficial or disadvantageous, depending on the application. For example, imidazolium ILs are used in hypergolic fuels,[63] and NHCs are thought to be involved in important steps of the spontaneous ignition process.[64] Better knowledge of the solvent/environmental conditions that lead to enhanced NHC content would be important for optimizing such processes. Beyond these energy and electrochemical applications, better characterization of NHC formation may allow ILs to find further use in novel organocatalysis applications.

Due to the difficulty of direct experimental measurement, computational approaches provide an important tool for investigating relative NHC stability in ILs and other environments. For example, equilibrium coefficients (e.g. for reaction 1) can be derived from reaction free energies computed from enhanced sampling molecular dynamics approaches; this of course assumes an approach that allows modeling the chemical reaction in the condensed phase (*vide supra*). As an illustration, in Figure 1 we show the free energy surface for reaction 1 in the *gas-phase*, projected along the bond breaking (C–H distance) and bond forming (O–H distance) coordinates (see Results for calculation details). This free energy surface highlights several important aspects about the carbene formation reaction. The reaction is observed to be barrierless, as is typically true for similar proton transfer reactions (in absence of solvent effects). The reactants ($EMIM^+$and acetate) are more stable than the products (NHC and acetic acid), but only by a relatively modest ~ 10 kJ mol^{-1} which implies significant fraction of all species in the gas phase. The global minimum occurs at $r_{CH} \approx 1.1$ Å and $r_{OH} \approx 1.8$ Å, within a broad minima basin that spans ~ 0.75 Å along the O–H coordinate. Because of the barrierless transition state, there is no local minima basin associated with the products, but rather they are inferred by approximate distance criteria of $r_{CH} > 1.6$ Å and $r_{OH} \sim 1.1$ Å. In the Supporting Information, we compare this free energy surface to the *potential energy surface*, and entropic effects are found to make only a relatively small quantitative contribution to the gas-phase

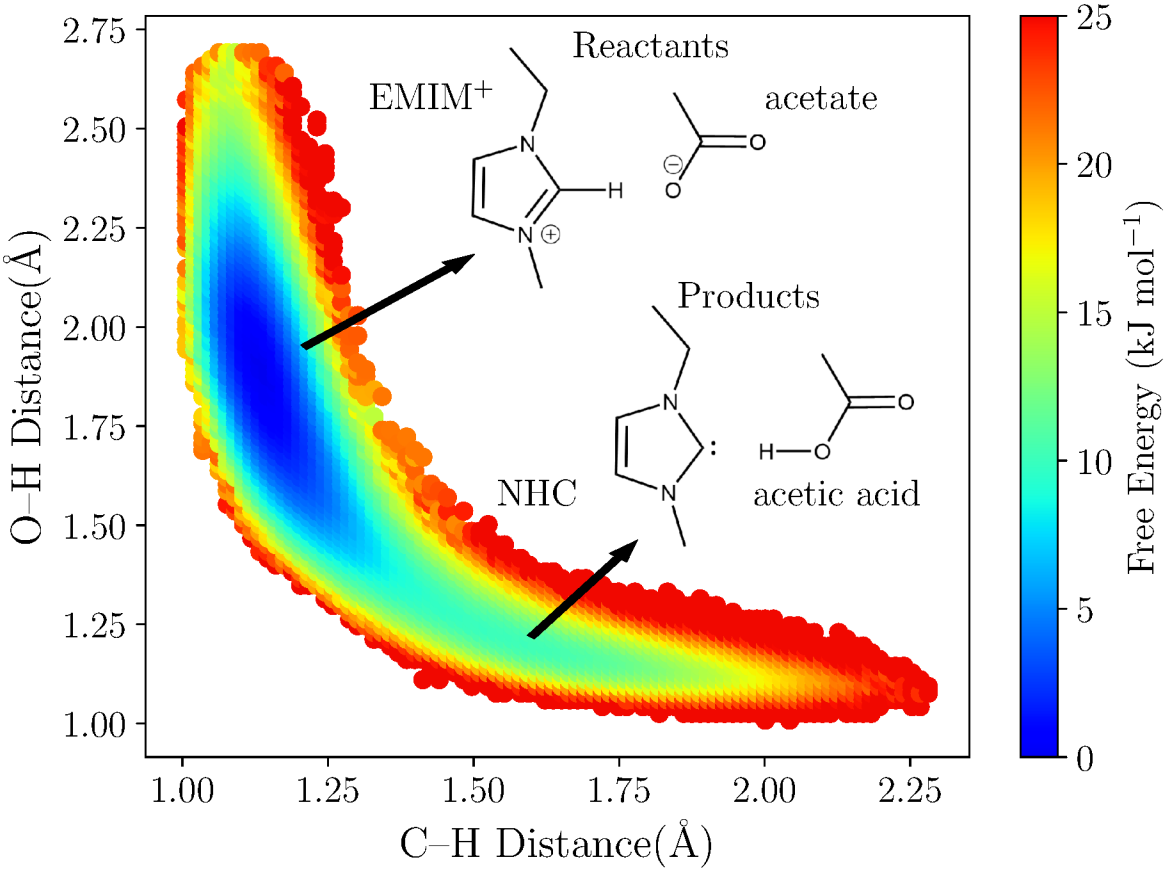

FIG. 1: Free energy as a function of C–H and O–H bond distance for the deprotonation of EMIM$^+$by acetate in the gas-phase. Arrows are drawn to the reactants and products to indicate their respective location on the surface.

reaction profile. Note that while Figure 1 indicates significant formation of carbene products in the gas-phase, large solvation energies of the reactant ions will substantially shift the equilibrium towards the reactants in solution. Developing a reactive force field that allows investigation of such solvent/environmental effects on the reaction free energy profile is the primary goal of this work.

In this paper, we develop a reactive force field for the carbene formation reaction (reaction 1) that combines both *physics-based* and *neural network* terms within an EVB approach. While neural networks and physics-based potentials have been combined before,[65–67] there are specific considerations for doing this within reactive force field development. Our approach, which we term "PB/NN potentials", is entirely general and is applicable to other chemical reactions in condensed phase environments. The ansatz of our PB/NN construction is the following: Physics-based

terms are utilized for all long-range intermolecular interactions, which ensures correct asymptotic behavior and facilitates transferability to various condensed-phase, solution environments. For the reacting complex, neural networks are utilized to describe all molecular vibrations in order to avoid inaccuracies associated with standard harmonic functional forms. In the transition state region, physics-based terms break down at close contact distances (e.g. Coulombic interactions), which is fixed by introducing short-range neural networks as residual corrections. Finally, the reactant and product "states" are coupled within an EVB-like Hamiltonian using a neural network for off-diagonal coupling which improves versatility and accuracy compared to analytic functional forms. The final PB/NN potential exhibits an accuracy of ~ 1 kJ mol^{-1} MAE for the reacting complex within the transition state region, and can be directly used in condensed phase, molecular dynamics simulations. Overall, more than 1 million electronic structure calculations were used to parameterize the final PB/NN potential. It is expected that this amount of training/parameterization data could be greatly reduced in future work, as we made no effort to optimize training data sampling/generation.

The manuscript is structured as follows: In the Methods section, we explain the motivation and construction of the PB/NN force field and our procedure to generate the necessary training data for parameterization. In the Results section, we validate each component of the force field, and present accuracy benchmarks by comparing to free energy profiles generated by AIMD simulations. While the overarching motivation is to explore solvent/environment effects on the carbene formation reaction, in this work we restrict analysis to systems that can be benchmarked with AIMD. Thus the "solvent" environment considered is a simple ionic cluster consisting of two additional solvating ions in addition to the reactant species. Investigation of this reaction in more complex condensed-phase environments will be the subject of future work.

II. METHODS

We first describe the general form of our PB/NN force field and the procedure for training and validating its individual components. We then discuss the electronic structure calculations used to generate the training data sets for the different force field components. Finally, we describe in detail the functional forms of the individual components of the force field and specific process for fitting each component.

A. General Functional Form

Our PB/NN force field has the generic functional form of a 2x2 Hamiltonian written in the basis of diabatic "reactant" and "product" states. This is similar to the empirical valence bond (EVB) method, multiscale-reactive molecular dynamics (MS-RMD) and other reactive force field approaches.[19,20,34,35,68–70] For a single step reaction, the total Hamiltonian and ground state energy are:

$$H_{PB/NN} = \begin{bmatrix} H_{11} & H_{12} \\ H_{12} & H_{22} \end{bmatrix} \tag{2}$$

$$E_g = \frac{1}{2}[(H_{11}+H_{22}) - \sqrt{(H_{11}-H_{22})^2+4H_{12}^2}] \tag{3}$$

The atomistic forces on each atom i are obtained using the Hellmann-Feynmann theorem in terms of the ground-state eigenvector (c_1, c_2)

$$F_i = -\sum_{m,n} c_m c_n \frac{\partial H_{mn}}{\partial r_i} \tag{4}$$

In Equation 2, the diagonal elements, H_{ii}, correspond to the "reactant" and "product" diabatic states, and the off-diagonal element ($H_{ij} = H_{ji}$) represents the coupling between these states. For the carbene formation reaction studied in this work, we refer to $EMIM^+$/acetate configuration as diabat 1, represented with H_{11}, and NHC/acetic acid configurations as diabat 2, represented with H_{22}. Throughout the method discussion, we use the terminology "solute" to refer to the reacting complex, and "solvent" to refer to an arbitrary chemical environment encompassing all non-reacting species. The diagonal elements H_{11} and H_{22} consist of the following terms, with subscripts identifying whether the energy contribution is specific to the reacting "solute" or the "solvent", and superscript indicating the type of interaction:

$$\begin{aligned} H_{ii} = E_{Solute}^{Morse} + E_{Solute}^{Intra,NN} + E_{Solute}^{Inter,NN} + E_{Solvent}^{Bonded,FF} \\ + E_{Solute,Solvent}^{Nonbonded,FF} + E_{Solute}^{\alpha} \end{aligned} \tag{5}$$

The terms E_{Solute}^{Morse} and $E_{Solute}^{Intra,NN}$ constitute the intra-molecular energy of the reacting complex in the specific diabatic topology; E_{Solute}^{Morse} is a Morse potential describing the chemical bond(s) that break/form during the reaction, and $E_{Solute}^{Intra,NN}$ represents all (non-reactive) intra-molecular vibrational energy contributions described by neural networks. The term $E_{Solvent}^{Bonded,FF}$ is the contribution

from standard harmonic bond, angle, and dihedral force field terms for all solvent molecules. The $E^{Nonbonded,FF}_{Solute,Solvent}$ refers to physics-based, force field terms accounting for all solvent-solvent, solute-solvent and solute-solute non-covalent, intermolecular interactions. These interactions must be corrected at short-range for the reacting species (e.g. transition state region) where the physics-based terms break down, and this correction is given by $E^{Inter,NN}_{Solute}$ modeled with a neural network. We note the subtle distinction between "*Intra*","*Inter*" and "*Bonded*","*Nonbonded*" labeling of the terms: $E^{Intra,NN}_{Solute}$ refers to the full intra-molecular energy of the solute molecules (albeit with/without the bond dissociation E^{Morse}_{Solute} term), whereas $E^{Bonded,FF}_{Solvent}$ is only part of the intra-molecular energy of solvent molecules, as there is additionally the usual contribution from non-bonded interactions ($E^{Nonbonded,FF}_{Solute,Solvent}$) for atoms separated by three or more bonds. Finally, E^{α}_{Solute} is the gas-phase electronic energy of the isolated monomers at infinite separation. The rationale and specific expressions used for each of these terms will be explained in further detail. It is important to note that solvent effects on the reaction energetics are mediated entirely by the $E^{Nonbonded,FF}_{Solute,Solvent}$ term, which in principle is given by an existing classical force field. This follows the ansatz of the EVB method, and implies that parameterization of the reactive force field (e.g. off-diagonal elements) can be done entirely based on the gas-phase potential energy surface of the reacting complex.[19,22]

For the H_{ij} off-diagonal coupling element, we utilize a neural network for enhanced accuracy and generality. We note that an alternative, analytic functional form would likely limit the extension of the model for more complex reactions, even if sufficient for the simple proton transfer reaction considered here.[28]. Utilizing a neural network for H_{ij} enables versatile description of complex energy dependence in a high dimensional coordinate space, and thus should be applicable for a wide variety of reaction coordinates. The exact structure of the H_{ij} neural network will be explained in detail in a later section.

B. Training Data Generation

Training data for the force field parameterization falls into three categories: 1) monomer DFT calculations, 2) dimer DFT calculations, and 3) dimer perturbation theory (SAPT0) calculations. Configurations were generated from (gas-phase) AIMD simulations of the $EMIM^{+}$/acetate (NHC/acetic acid) reaction complex, which were then input to the three types of calculations. To parameterize a reactive force field, it is essential to generate sufficient training data in the transi-

tion state region. Because the carbene formation reaction is barrierless (Figure 1), the transition state (and proton transfer reactions) is adequately sampled by direct AIMD simulations of 1-10 ps trajectories. For a more complex reaction with significant reaction barrier, enhanced sampling approaches would be necessary to generate sufficient training data spanning the transition state region.

For the AIMD simulations, the QUICKSTEP method in the CP2k software package was used,[10] with PBE-D3(BJ) density functional and a mixed Gaussian/plane-wave basis set.[71–73] The basis set consisted of the aug-DZVP Gaussian atomic basis set, a cutoff of 280 Ry to expand the auxiliary electron density and Goedecker-Teter-Hutter pseudopotentials for the core electrons.[74] The Pulay mixing scheme is used for SCF convergence, with a convergence criterion of 10^{-7} au.[75] We run NVT simulations using a Langevin thermostat at 300, 400, 500 and 600K of each of the individual monomers and the dimer, with the higher temperatures allowing sampling of higher energy configurations. A 0.005 fs^{-1} friction coefficient was used for these simulations, with a 1.0 fs timestep for integrating the nuclear equations of motion.

The Psi4 electronic structure package was then utilized to generate training data from these AIMD configurations.[76] For the DFT calculations, we use the PBE-D3(BJ)/aug-cc-pVTZ level of theory. Calculations employing the SAPT0/aug-cc-pVTZ flavor of symmetry adapted perturbation theory were conducted for geometries in the dimer training set; here, the dimers were partitioned into either diabat 1 ($EMIM^+$/acetate) or diabat 2 (NHC/acetic acid) configurations for defining the SAPT0 monomer wavefunctions. Note that the commonly employed δE_{HF} term in SAPT0 is excluded, for reasons discussed later. Table I summarizes the different training datasets that were constructed, including the number of geometries/configurations in each dataset, the type of calculation, and whether energies/forces were calculated. In addition, this table lists the type/architecture of the neural network that each dataset was used to train, along with the number of atomic degrees of freedom built in to the corresponding neural network; such details are explained in the following sections. Throughout the remainder of the work, each dataset will be referenced by its corresponding number given in the first column of Table I. We note that over 1 million monomer/dimer geometries/configurations were used in the training data generation. Because we made no attempt to optimize or reduce the amount of training data, it is likely that significant reductions could be achieved with more efficiently designed data generation approaches.

dataset no.	reference data	# of calculations	Neural Network	Architecture	Atomic DOF
1	$EMIM^+$DFT energies/forces	403625	$CNN_{(EMIM^+)}$	SchNet	19
2	Acetate DFT energies/forces	406173	$CNN_{(OAc^-)}$	SchNet	7
3	NHC DFT energies/forces	404705	$CNN_{(NHC)}$	SchNet	18
4	Acetic acid DFT energies/forces	421764	$CNN_{(AcOH)}$	SchNet	8
5	Dimer DFT energies/forces	226075	H_{12}	AP-Net	26
6	$EMIM^+$/acetate SAPT0 energies	427004	$H_{11} : E_{Solute}^{Inter,NN}$	AP-Net	26
7	NHC/acetic acid SAPT0 energies	265343	$H_{22} : E_{Solute}^{Inter,NN}$	AP-Net	26

TABLE I: Summary of training data sets, including type and number of calculations in each set. Each data set is used to parameterize a particular neural network within the force field; the neural network architecture is listed as well as the number of atomic degrees of freedom that the neural network depends on (note that the total degrees of freedom is equal to 3N-6, with N equal to the number of atoms).

C. Force Field Components

1. Bonded Force Field Terms (E_{Solute}^{Morse} and $E_{Solvent}^{Bonded,FF}$)

The bond formation/dissociation that occurs during the reaction is modeled with Morse potential(s)

$$E_{Solute}^{Morse} = D(1 - e^{-a(r-r_o)})^2 \tag{6}$$

In our case, we use two Morse potentials for the bonds involved in the deprotonation reaction; one is for the C–H bond of $EMIM^+$in diabat 1 (H_{11}), and the other is for the O–H bond of acetic acid in diabat 2 (H_{22}). As will be discussed in Section III A, there are distinct advantages to separating out these bond dissociation/formation coordinates from the rest of the intramolecular energy (within $E_{Solute}^{Intra,NN}$). The Morse potentials provide a physical way to account for this bond breaking/forming energy, with correct asymptotic behavior, while a neural network would not correctly extrapolate to the bond dissociation limit unless explicitly trained in that region. In short, using Morse potentials for dissociation coordinates restricts the remaining intra-molecular energy term $E_{Solute}^{Intra,NN}$ to a much smaller region of phase space (non-dissociative vibrations) which

is important for stability of the neural network (and force field). Fitting the Morse potentials involves straightforward bond dissociation scans, and the resulting parameters are found in Table S1 of the Supporting Information.

The bonded terms for the solvent molecules comprising $E_{Solvent}^{Bonded,FF}$ are standard harmonic bond, angles, and dihedral terms and thus require no elaboration. In general, these may be taken from standard, existing force fields.[77–79] In this particular case, the solvent that we study is $EMIM^+$and PF_6^- ions (Section III D), and bonded parameters are taken from previous work.[80,81]

2. *Intramolecular Neural Network ($E_{Solute}^{Intra,NN}$)*

For the reacting "Solute" complex, we use a neural network for each monomer to capture all intra-molecular energetics besides the explicit bond dissociation (the latter accounted for by E_{Solute}^{Morse}). The motivation for this is that standard harmonic bond, angle, and dihedral potentials introduce errors on the order of $\sim$ 10 kJ mol^{-1} or larger for these energetic contributions near the transition state region, which would likely preclude chemical accuracy (Section III A). In Figure S2 of the Supporting Information, we show an example of the error introduced when a standard bonded potential is alternatively used for the reacting complex. In contrast, the neural networks provide very accurate renderings of $E_{Solute}^{Intra,NN}$, with errors on the order of ~ 0.1 kJ mol^{-1} as demonstrated in Section III A.

The SchNet architecture is used to train convolution neural networks (CNNs) for each monomer in the reacting complex.[82] The CNN architecture within SchNet has previously been shown to provide accurate potential energy surfaces of isolated molecules.[82] Specifically, $E_{Solute}^{Intra,NN}$ for H_{11} and H_{22} are given by

$$H_{11} : E_{Solute}^{Intra,NN} = CNN_{(EMIM^+)} f(r_{CH}) + CNN_{(OAc^-)} \tag{7}$$

$$H_{22} : E_{Solute}^{Intra,NN} = CNN_{(NHC)} + CNN_{(AcOH)} f(r_{OH}) \tag{8}$$

with

$$f(r) = \frac{1}{(e^{\beta(r-\mu r_o)} + 1)} \tag{9}$$

The output of the CNN is thus multiplied by a Fermi-Dirac like damping function for the monomers with dissociative bonds. The argument of the damping function is the length of the dissociating bond, e.g. r_{CH} for $EMIM^+$and r_{OH} for acetic acid. The motivation is that these neural networks will predict uncontrolled values in the dissociated regime which is outside the scope of

the training data. Introduction of the damping function does not adversely effect the accuracy of the force field; in the damped regime, the bond dissociation energy E_{Solute}^{Morse} is very large, and thus the contribution of this diabat to the total energy will be small. The parameters of the damping function are found in Table S2 of the Supporting information. Specifically, r_o, is the equilibrium bond length, and μ is a "scaling factor" for which we assign the value $\mu = 2.25$, so that the damping occurs at just over twice the equilibrium bond length.

Datasets 1-4 in Table I are used to train the monomer CNNs in Equations 7 and 8. Before training, all energies are converted to relative values by subtracting off the energy of the minimized monomer geometry. For the monomers with an E_{Solute}^{Morse} contribution, we fit to the energy difference between the QM energy and Morse energy. Because the damping function doesn't "turn on" until approximately twice the equilibrium bond length, the $CNN_{(EMIM^+)}$ and $CNN_{(AcOH)}$ which involve bond dissociation coordinates must be fit to an expanded dataset. To fit these specific monomers, Datasets 1 and 4 are supplemented with "dissociation" configurations from Dataset 5 in which the appropriate bond is stretched to distances longer than twice the equilibrium bond length. The importance of adding such additional "dissociation" data will be further discussed in the Results section. The hyperparameters used to train the CNNs are similar to default SchNet values,[82] and are explicitly discussed in the Supporting Information. We use the combined energy and force mean-squared error loss function from Schütt *et al.* [82] in order to train the neural networks (shown in Equation S1 in the Supporting Information).

3. *Nonbonded Force Field ($E_{Solute,Solvent}^{Nonbonded,FF}$) and Intermolecular Neural Network ($E_{Solute}^{Inter,NN}$)*

In principle, any standard force field could be utilized for the diabatic $E_{Solute,Solvent}^{Nonbonded,FF}$ terms, which contain contributions from all nonbonded interactions. We choose to use the SAPT-FF force field[83,84] for $E_{Solute,Solvent}^{Nonbonded,FF}$, which has been previously developed based on symmetry adapted perturbation theory calculations. The SAPT-FF force field utilizes Drude oscillators to model electronic polarization, meaning that polarization is explicitly included in the $E_{Solute,Solvent}^{Nonbonded,FF}$ terms; the complete functional form can be found in the work of McDaniel and Schmidt [84]. SAPT-FF has been demonstrated to be very accurate for organic ions constituting ionic liquids,[85,86] such as the species studied in this work.

The SAPT-FF parameters for each monomer are listed in Tables S3-S6 of the Supporting Information. A virtual site was added to acetate in order to better describe the electrostatic interactions,

as described in the Supporting Information. The $EMIM^+$and NHC monomers share the same parameters, except for those associated with the reactive sp^2 carbon; we adjusted these parameters in order to better fit NHC/acetic acid SAPT0 energies, which we show in Figure S10 of the Supporting Information. All intra-molecular, nonbonded interactions within the reacting "Solute" complex are purposely excluded, as the full intra-molecular energy is captured in the $E_{Solute}^{Intra,NN}$ term. For the solvent, 1-4 and greater intra-molecular nonbonded interations are included in the standard way. It is well-known that Drude oscillator models exhibit "polarization catastrophe" at short distances/large electric fields.[87] Without modification, this would inevitably be problematic for a reactive force field in the transition state region at short atom-atom contact distances. To fix this issue, we introduce an anharmonic restraining potential on each Drude oscillator in order to avoid polarization catastrophe, as described in Huang *et al.*[88]. Further details of the Drude oscillator approach are given in the Supporting Information.

Standard force fields account for long-range interactions (i.e. electrostatics, dispersion), and short range repulsion, and are designed to be accurate at van der Waals (VDWs) contact distances. At distances much shorter than the VDWs contact distance, these force fields will inevitably break down due to their limiting functional forms.[89,90]. To ensure accuracy of the diabatic H_{11} and H_{22} terms within the transition state region, we thus supplement $E_{Solute,Solvent}^{Nonbonded,FF}$ with a "correction" term, $E_{Solute}^{Inter,NN}$. The $E_{Solute}^{Inter,NN}$ term is only for the reacting "Solute" species, and is modeled by a neural network; it is designed to compensate for breakdown of the analytic functional forms within $E_{Solute,Solvent}^{Nonbonded,FF}$ that occur at distances significantly shorter than the VDWs contact distance (i.e. within transition state region).

Care must be taken to parameterize $E_{Solute}^{Inter,NN}$ consistently with the diabatic representation ansatz of the force field (Equation 2). As $E_{Solute}^{Inter,NN}$ enters into the diagonal elements (H_{11}, H_{22}), it should not include orbital interactions related to breaking/forming chemical bonds, the latter of which are accounted for by the off-diagonal coupling, H_{12} . The standard approach for parameterizing diabatic Hamiltonian terms is using constrained DFT.[19,22,91] Here, we propose to use symmetry adapted perturbation theory instead, in the form of SAPT0. Our choice of SAPT0 is for two reasons: First, it is consistent with the SAPT-FF force field used for $E_{Solute,Solvent}^{Nonbonded,FF}$, and second, it provides a mechanism for interpretting solvent effects on the reaction profile utilizing the explicit energy decomposition.[92] We note that SAPT0 generally incorporates a variational "delta-Hartree Fock" (δE_{HF}) correction to the interaction energy.[93] Here, we exclude the δE_{HF} term to avoid variational energy contributions in the diabatic parameterization.[90] The criteria for a "good" dia-

batic state definition in the context of a reactive force field is the capability of accurately capturing solvation effects on the reaction profile; this is benchmarked for our approach in Section III D.

The $E_{Solute}^{Inter,NN}$ term is then parameterized to the residual difference between SAPT0 energies and the energy contribution of $E_{Solute,Solvent}^{Nonbonded,FF}$. Specifically datasets 6 and 7 listed in Table I are employed for this parameterization. A subtle issue is that SAPT0 was used to generate datasets 6 and 7, while DFT-SAPT was primarilly used in prior parameterization of SAPT-FF for the $E_{Solute,Solvent}^{Nonbonded,FF}$ term;[80,84] this leads to a minor discrepancy between levels of theory. For the calculations in this work, we have utilized SAPT0 purely for reasons of computational efficiency, and the small errors introduced relative to a higher-level method will be discussed within the context of analyzing our results (Section III D).

We utilize a different neural network architecture for $E_{Solute}^{Inter,NN}$ than was used for the $E_{Solute}^{Intra,NN}$ terms in Section II C 2. The AP-Net neural network architecture[94] is used for $E_{Solute}^{Inter,NN}$, which partitions the total energy into contributions from *atom pairs* (rather than *individual atoms*) and thus is compatible with typically used pairwise interaction energy expansions. Importantly, we find that AP-Net provides a much smoother potential energy surface for intermolecular interactions compared to other neural network architectures (see Supporting Information), which is an essential requirement for use in MD simulations. We modify the AP-Net output slightly from the original work,[94] to explicitly restrict the energy contribution to configurations where the molecules are at close range (≤ 4Å):

$$E_{Solute}^{Inter,NN} = \sum_{i \in A, j \in B} (E_{ij} f_c(r_{ij})) f(r_{bond}) \tag{10}$$

$$f_c(r_{ij}) = \begin{cases} \frac{1}{2}(cos(\frac{\pi r_{ij}}{r_c}) + 1) & r_{ij} \leq r_c \\ 0 & r_{ij} > r_c \end{cases} \tag{11}$$

Here, E_{ij} is the pairwise energy contribution predicted by the neural network (equivalent to ΔE_{ab} labeled in Glick *et al.*[94]) and the cutoff function $f_c(r_{ij})$ is applied to pairs of atoms in the dimer and is the same form as that commonly used for gathering the atomic neighbors in many neural network frameworks.[40,94] For example, if an atom pair has a distance larger than r_c, then the particular pairwise energy is zero. This restricts $E_{Solute}^{Inter,NN}$ to only correct the interaction energy between dimers at relatively close distances. The $f(r_{bond})$ is the same Fermi-Dirac damping function as in Equation 9, and is a function of the dissociating bond length of the particular diabat. This

additional damping function zeroes the $E_{Solute}^{Inter,NN}$ energy contribution when the bond has stretched too far (and the system has switched to the opposite diabat). The parameters for the Fermi-Dirac functions used for the $E_{Solute}^{Inter,NN}$ neural networks are given in Table S7 of the Supporting Information.

The majority of the hyperparameters used in the construction of the $E_{Solute}^{Inter,NN}$ neural network are the default values given in Glick *et al.* [94]. The small differences in our present implementation are as follows. While the ReLU activation function was used in the original AP-Net paper, we use the shifted softplus activation function as implemented in SchNet.[82] We set ρ in Equation S1 to 1, as we are only fitting energies in this case. We also use a batch size of 100 for training as we used for training the intramolecular neural networks, and we used the same learning rate decay procedure as mentioned earlier, except we start with an initial learning rate of 5.0 x 10^{-4} due to observing improved results. Our train-test-validation split was the same as was used for the intramolecular neural networks.

4. H_{12} Neural Network

We lastly discuss the H_{12} coupling term, which is also modeled with a neural network. As noted by Chang and Miller [70], it is only necessary to define H_{12} for the intermediate transition state region between reactants and products; the system is well-described by the diagonal elements of the Hamiltonian for asymptotic reactant and product configurations, and H_{12} may be set to zero. We use a similar pairwise representation and neural network architecture as AP-Net to model H_{12}; however, we no longer restrict the pairs of atoms to be in different monomers, as there is no way to distinguish between monomers while the reaction is occurring.

$$H_{12} = (|\sum_{i,j\neq i} E_{i,j}|) f_c(r_{CH}) f_c(r_{OH}) \tag{12}$$

Here, labels 'i' and 'j' indicate any atom in the reacting complex. The absolute value of the sum of pairwise energies from the neural network is taken in order to ensure that H_{12} is strictly positive. The neural network output is also multiplied by Fermi-Dirac functions with both bond distances, r_{CH} and r_{OH}. This ensures that the off-diagonal element will be zero and that the total energy will follow the lowest energy diabatic state in the asymptotic limit. The parameters for the Fermi-Dirac function are the same as those used for $E_{Solute}^{Inter,NN}$ Our procedure for identifying configurations from the DFT dimer dataset 5 to use for training H_{12} is described in the Supporting Information Figure

S8, and we also explain how to obtain energies and forces from these configurations suitable for training H_{12} in the Supporting Information. The structures in dataset 5 have geometries that fall within the range of the Fermi-Dirac damping functions i.e. have C–H distances less than the cutoff distance for the C–H damping function and O–H distances less than the cutoff for the O–H damping function. We use the same loss function as was used for training $E_{Solute}^{Intra,NN}$, and the hyperparameters for the neural network are the same as were used for training $E_{Solute}^{Inter,NN}$.

III. RESULTS AND DISCUSSION

We organize the discussion of our results as follows. In Sections III A and III B, we first discuss accuracy benchmarks of the different force field components. Within this discussion, the rationale for our particular choice of force field components is elucidated by comparison to alternative choices/models. In Section III C, we evaluate the accuracy of the total PB/NN force field within the transition state region of the reacting complex. Lastly in Section III D, we evaluate the ability of the force field to accurately capture solvent effects on the reaction profile. This is benchmarked by computing reaction free energies with and without the presence of a "model" solvation environment, and comparing to explicit AIMD free energy predictions.

A. Intramolecular Neural Network ($E_{Solute}^{Intra,NN}$)

In Figure 2, we show the energy predictions of the intramolecular neural networks compared to DFT relative energies for each monomer involved in the reaction. The test sets have approximately 20,000 structures for each monomer sampled from datasets 1-4 in Table I, with the test data not included in the training data. The energy from the Morse potential is added to $E_{Solute}^{Intra,NN}$ for $EMIM^+$and acetic acid to obtain the total energy. The energy MAEs for each figure are listed in the figure; they are also listed in Table S8 along with the force MAEs. The largest energy MAE is 0.34 kJ mol^{-1} for $EMIM^+$, as well as the largest force MAE of 0.85 kJ mol^{-1} Å^{-1}. These errors are comparable to those computed by SchNet neural networks for similarly sized molecules.[82] For acetate and NHC, the two monomers that do not have a reacting bond, there are no significant outliers. In contrast, there are a few outliers for $EMIM^+$and acetic acid that occur for configurations with the C–H and O–H bond dissociated, respectively. For these configurations, the Fermi-Dirac functions in Equation 9 damp the neural network prediction and lead to the associated errors. Note

however that these outliers are at very high energy (above 400 kJ mol^{-1}), and thus will not affect the accuracy of the full PB/NN potential (the system will have switched to the opposite diabatic state).

As mentioned, there is a significant improvement in accuracy for $E_{Solute}^{Intra,NN}$ when using neural networks compared to typical force field expressions. This is demonstrated in Figure S2 of the Supporting Information. Standard force field expressions (harmonic bonds, angles, dihedrals) would introduce errors of at least several to tens of kJ mol^{-1} even after optimizing the parameters. This introduced error would have one of two effects; it would either hinder the total accuracy of the force field, or these errors would be compensated when fitting the H_{12} coupling term to the adiabatic surface. If the latter case, then H_{12} would have diminished physical meaning for the diabatic representation. At this point, one can only speculate how this would effect the ability to capture solvent effects in the condensed phase and/or the stability of the neural network.

The need for the Morse potential for EMIM$^+$and acetic acid monomers is shown in Figure S4 and S5. We compare predicted energies for bond dissociation scans of EMIM$^+$and acetic acid for two different neural networks trained to datasets 1 and 4 in Table I; one has been trained to residual energies including the Morse potential, and the other is trained "stand-alone". While the stand-alone neural network accurately predicts the QM energy for short bond distances, it produces severe, uncontrolled errors for longer bond lengths toward the dissociation limit. Clearly, such error would be unacceptable in a working reactive force field. While presumably this issue could be fixed by introducing more training data in the dissociation region, there are practical difficulties such as SCF instability, etc., and supplementing with a Morse potential is likely the best solution. The final intra-molecular potential including the Morse potential and damped CNN accurately reproduce the bond dissociation scans, as shown in Figure S5.

We note that it is important to include stretched geometries sampled from the dimer AIMD simulations to the training datasets 1-4 in Table I for all monomers. As mentioned, the intra-molecular neural networks for EMIM$^+$and acetic acid are damped at approximately twice the equilibrium bond length, and so training data spanning this regime is included in datasets 1 and 4 (Table I) to ensure stability of the neural networks.

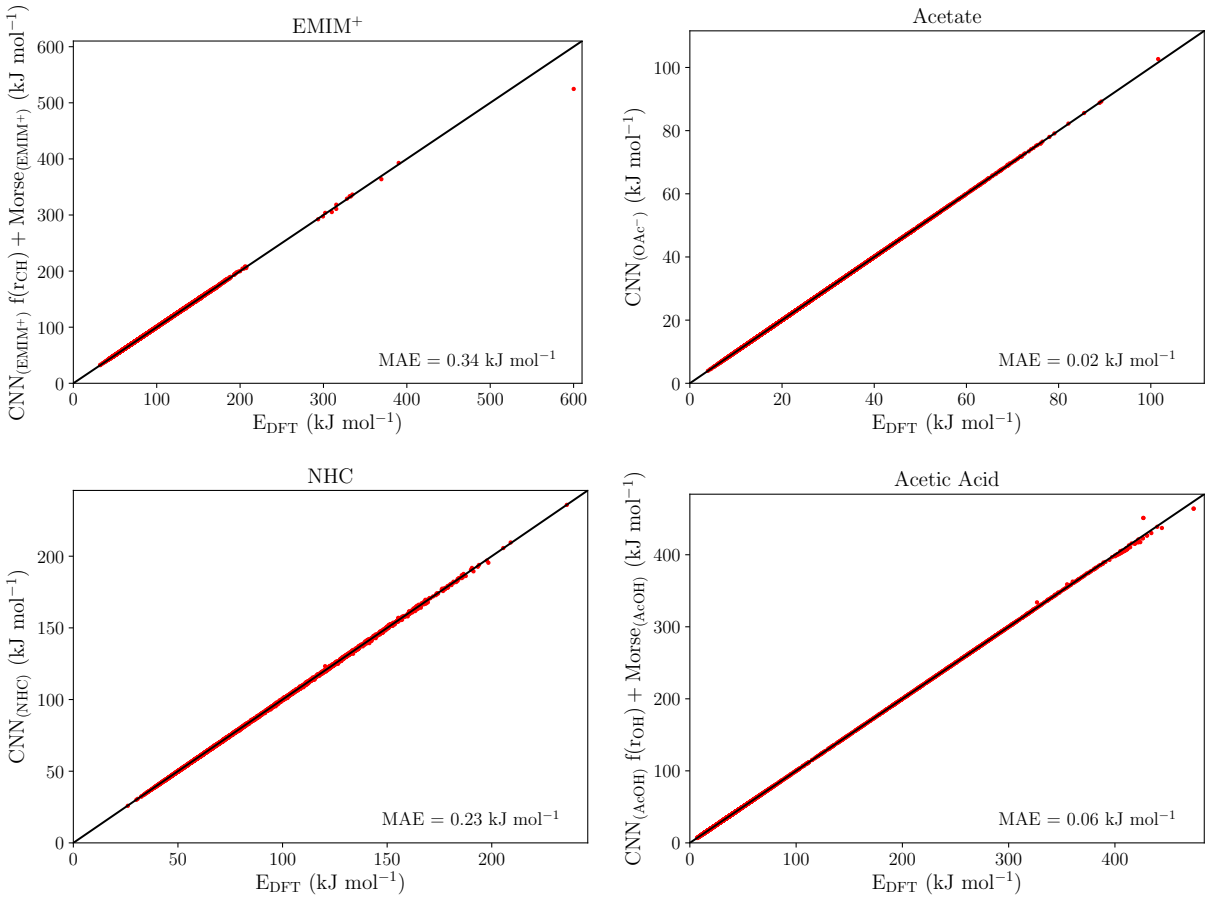

FIG. 2: PBE-D3(BJ)/aug-cc-pVTZ vs. neural network energy predictions for each monomer involved in the reaction. We have added E^{Morse}_{Solute} to the neural network prediction for EMIM$^+$and acetic acid. Each plot shows 5000 randomly-selected structures from the test set; the MAE listed corresponds to the full test set for each monomer.

B. Nonbonded Force Field ($E^{Nonbonded,FF}_{Solute,Solvent}$) and Intermolecular Neural Network ($E^{Inter,NN}_{Solute}$)

As discussed in the Methods section, the $E^{Inter,NN}_{Solute}$ term is designed to be a short-range correction to the SAPT-FF intermolecular interactions ($E^{Nonbonded,FF}_{Solute,Solvent}$) for the reacting complex. In Figures S9 and S10, we show the accuracy of SAPT-FF for describing intermolecular interactions for *non-reactive configurations* of the dimer (see Supporting Information for details). It is clear that the accuracy for these configurations is fairly good, on par with previous work for this specific force field.[80,84] However, the accuracy of SAPT-FF breaks down for close range "reactive" configurations in dataset 5 (Table I) generated from the AIMD simulations. This breakdown is expected due to limitations in functional form, as these configurations are significantly closer than

the VDWs contact distance. The motivation for adding the $E_{Solute}^{Inter,NN}$ term is to improve the diabatic energy (as compared to SAPT0) for such close distances within the transition state regime.

In Figure 3, we benchmark the total intermolecular interaction energy, $E_{Solute}^{Inter,NN} + E_{Solute}^{Nonbonded,FF}$, compared to test data taken from datasets 6 and 7 in Table I. For greater insight, we have divided each test set into 3 different subsets to illustrate the accuracy at distinct regions of the potential energy surface. The three subsets are generated by computing the diabatic expansion coefficient "c_1" for each configuration utilizing the final Hamiltonian. The first subset corresponds to the "Diabat 1" region, categorized by $c_1^2 > 0.8$; the second subset is the "Transition State" region, corresponding to $0.2 < c_1^2 < 0.8$; and the third subset is the "Diabat 2" region, corresponding to $c_1^2 < 0.2$. In Figure 3, we show the MAE of $E_{Solute}^{Inter,NN} + E_{Solute}^{Nonbonded,FF}$ for the three regions, for both H_{11} and H_{22} force field elements. In Figure S11 of the Supporting Information, we show corresponding plots for the stand-alone force field energy ($E_{Solute}^{Nonbonded,FF}$); thus comparison of Figure 3 and Figure S11 indicates the contribution of the neural network term, $E_{Solute}^{Inter,NN}$. The $E_{Solute}^{Inter,NN}$ term greatly improves the agreement with the SAPT0 energies compared to the test sets. The effect is most significant in the transition state region and dissociation limit, where the force field is clearly expected to breakdown. Figure S11 indicates that the stand-alone force field terms ($E_{Solute}^{Nonbonded,FF}$) of both H_{11} and H_{22} lose predictive ability in the transition state region. The neural network ($E_{Solute}^{Inter,NN}$) substantially improves accuracy in all regions of the potential energy surface, for both H_{11} and H_{22} force field elements. The most pertinent MAE is for the particular subset in which the diabatic region and Hamiltonian element correspond, i.e. $H_{11} \Leftrightarrow$ "Diabat 1", and $H_{22} \Leftrightarrow$ "Diabat 2"; here, the MAEs are 1.32 kJ mol^{-1} and 0.50 kJ mol^{-1} respectively. Furthermore, corresponding MAEs within the transition state region are 1.34 kJ mol^{-1} and 0.73 kJ mol^{-1}, which is also well within chemical accuracy. The only significant breakdown occurs in regions where the Hamiltonian element and diabat do not correspond, e.g. $H_{22} \Leftrightarrow$ "Diabat 1", which has MAE = 8.28 kJ mol^{-1}. However, for this region the contribution to the total energy from H_{22} diminishes to the extent that the error is largely inconsequential.

The potential energy surface generated by $E_{Solute}^{Inter,NN}$ must be smooth in order to run MD simulations. As noted by Glick *et al.*[94], neural network potentials that utilize a sum of atom energies to represent the total energy often do not generate smooth potential surfaces for intermolecular interactions, leaving them unsuitable for running MD simulations. While our final working $E_{Solute}^{Inter,NN}$ terms employ AP-Net type neural network architectures (Section II C 3), the SchNet architecture was also tested in preliminary stages of the force field development. In Figure S12

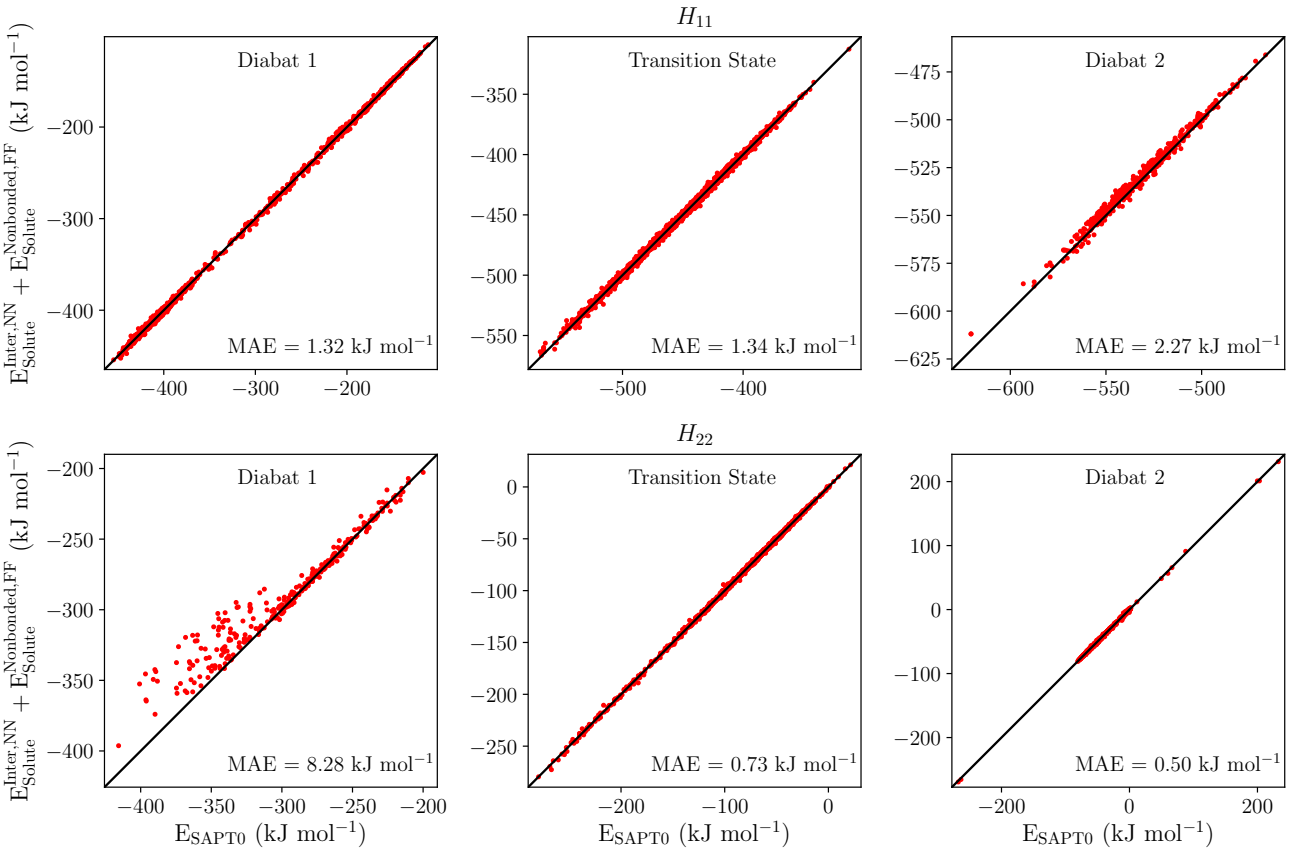

FIG. 3: SAPT0 vs. $E^{Inter,NN}_{Solute} + E^{Nonbonded,FF}_{Solvent}$ predictions for both H_{11} and H_{22}. Diabat 1, Transition state and Diabat 2 regions are defined with respect to their value of c_1^2 as discussed in the main text.

and S13 of the Supporting Information, we compare scans of $E^{Inter,NN}_{Solute}$ for [EMIM$^+$][OAc$^-$] as predicted with either the SchNet or AP-Net architecture. For the SchNet architecure, the scan is not smooth and exhibits somewhat uncontrolled behavior at longer distances. In contrast, the $E^{Inter,NN}_{Solute}$ term constructed from the AP-Net architecture exhibits smooth behavior over the full scan region. The final, $E^{Inter,NN}_{Solute} + E^{Nonbonded,FF}_{Solute}$ term thus utilizes the AP-Net architecture, with the $E^{Inter,NN}_{Solute}$ contribution damped at longer distances, such that the total intermolecular interaction energy asymptotically matches SAPT0 *ab initio* values.

C. PB/NN Force Field Total Energy

In the previous Sections III A and III B, the intra- and inter-molecular components of the diagonal H_{11} and H_{22} force field terms were benchmarked and discussed. The final stage in the PB/NN

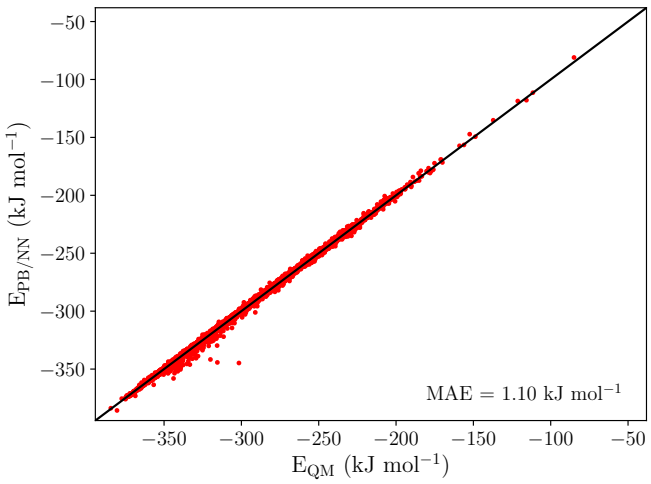

FIG. 4: PBE-D3(BJ)/aug-cc-pVTZ energies vs the force field $H_{PB/NN}$ energies with C–H bond distances less than 1.8 Å and O–H bond distances less than 1.8 Å. The plot shows 5000 randomly-selected structures from the test set; the MAE listed corresponds to the full test set.

force field development is parameterization of the H_{12} off-diagonal coupling to the adiabatic potential energy surface (dataset 5, Table I). As discussed in Section II C 4, the H_{12} term consists of an AP-Net type neural network architecture. In Figure 4, we compare the total PB/NN energy (Equation 3) to test set energies from dataset 5 in Table I; this comparison effectively demonstrates the accuracy of the H_{12} neural network. We note that in this comparison, the energies of the isolated monomers in their equilibrium geometries have been subtracted out (i.e. relative energies). The MAE for these configurations is 1.10 kJ mol^{-1}, which is within chemical accuracy. Furthermore, the force field matches well with DFT energies for high energy configurations, approximately 250 kJ mol^{-1} above the minimum. We list the energy MAE with the force MAE in Table S9 in the Supporting Information. The force MAE is 2.55 kJ mol^{-1} Å^{-1}, demonstrating high fidelity in force predictions as well. In Figure S14 (Supporting Information) we also show DFT vs. PB/NN energy comparison from an MD trajectory, which gives a similar MAE of 1.14 kJ mol^{-1}.

The primary motivation for the diabatic representation utilized within our PB/NN force field is to enable direct incorporation of solvent effects in condensed-phase simulations. In this context, it is insightful to analyze the diabatic decomposition of the final force field after H_{12} parameterization (Figure 4). In Figure 5, we reproduce the AIMD free energy surface of the gas-phase reaction alongside a plot of the expansion coefficient c_1^2 of the reactant (EMIM$^+$/acetate) state. The con-

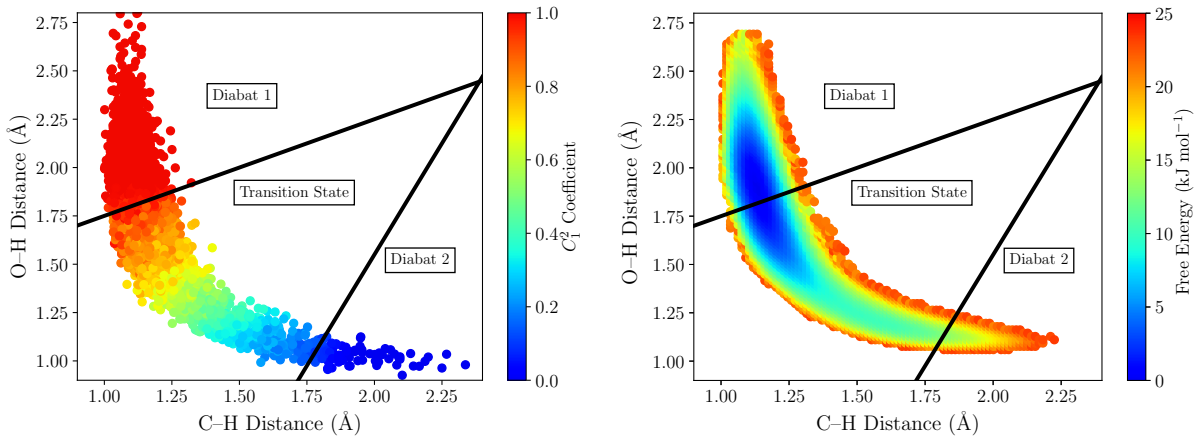

FIG. 5: a) Diabatic expansion of PB/NN force field in terms of c_1^2 coefficient, compared to b) reaction free energy surface projected onto C–H and O–H bond distances Configurations are taken from dataset 5 in Table I, and the lines drawn in the plot qualitatively separate the diabat 1, diabat 2, and transition state regions.

figurations in Figure 5 are from dataset 5 in Table I, and the reaction coordinate is projected onto the C–H and O–H bond distances. It is evident that the diabatic representation of the force field matches the respective "reactant", "transition state", and "product" regions of the reaction free energy surface. The wide minimum in the free energy profile (dark blue region, Figure 5b) corresponds to the EMIM$^+$/acetate "reactant" state with O–H distance approximately greater than 1.5 Å. For this region, the force field predicts values of $c_1^2 > 0.8$, indicating that the system is mostly composed of the EMIM$^+$/acetate "reactant" state. Indeed, at the center of this minimum region, the force field predicts values close to $c_1^2 = 1$ corresponding to pure EMIM$^+$/acetate reactant. Figure 5a) clearly indicates the transition between diabatic states in the force field representation as the reaction proceeds through the transition state region. At intermediate values for both C–H and O–H bond lengths, the force field predicts a mixed state consisting of significant fraction of both "reactant" and "product" diabats. For example, the center of the "transition state" region with $c_1^2 = 0.5$ (and $c_2^2 = 0.5$) is roughly located at $r_{OH} = 1.25$ Å and $r_{CH} = 1.35$ Å. As the reaction continues to longer C–H distances (and shorter O–H distances), the force field gives small c_1^2 values, indicating that the system has largely transitioned to the product diabatic state. For $r_{CH} > 1.8$Å, the system is essentially entirely composed of the product diabat, with $c_1^2 = 0$ (and c_2^2=1).

The analysis in Figure 5 confirms that the force field gives a physically meaningful description

of the reaction profile in terms of "reactant" and "product" diabatic states. The diabatic representation was parameterized to SAPT0 calculations (II C 3), and the realistic nature of the force field's diabatic expansion lends merit to this approach. However, the essential test of the diabatic representation is the ability for the force field to accurately capture solvent effects on the reaction profile. This criteria is benchmarked next, for which we consider a "model" solvation environment that is amenable to explicit AIMD benchmark calculations.

D. $EMIM^+$/Acetate Reaction Free Energies with/without "Solvation" Environment

We now benchmark the ability of the PB/NN force field to capture solvent effects on the $EMIM^+$/acetate reaction profile. For this purpose, we consider a "model" solvation environment consisting of a gas-phase ion cluster. This choice enables tractable AIMD simulations, whereas explicit AIMD benchmarks would be intractable for alternative liquid phase environments. Our "model" solvation environment is a four ion cluster, created by adding two additional ions, $EMIM^+$cation and PF_6^- anion, to the $EMIM^+$/acetate reacting dimer. The PF_6^- anion is not basic and cannot deprotonate $EMIM^+$, which is the motivation for adding this species rather than another acetate anion. While this "model" solvation environment is clearly not the same as a liquid or condensed phase system, the surrounding ions will create large electric fields felt by the reacting complex. We thus believe that this provides a good test of the force field's ability to capture modulation of the reaction profile by external electric fields, while simultaneously enabling tractable AIMD benchmarks.

We compute free energy reaction profiles with both the PB/NN force field and also explicit AIMD simulations. Potentials of mean force (PMFs) are computed as a function of two coordinates, namely the C–H and O–H (reacting proton) distances, using umbrella sampling. The umbrella sampling utilized harmonic potentials with a 0.01 au force constant. The C–H and O–H distances at which the umbrella potentials are centered are described in the Supporting Information. Each simulation window was started with an initial configuration from an equilibrated simulation of the previous window. The Weighted Histogram Analysis Method (WHAM) was used in order to compute the PMF from the umbrella sampling simulations.[95] Free energy profiles were computed for both the isolated reacting complex (two ion system), as well as with the "model" solvation environment (four ion system). For the two ion system, each window consisted of 40-50 ps simulations, with 5 ps used as equilibration. For the four ion system, the simulations for each win-

dow were run for ∼200 ps, with 10 ps used as equilibration. The AIMD simulations were run at 300K in CP2k, using the same simulation settings as mentioned in the Methods section. The force field simulations were run using an ASE calculator;[96,97] the calculator combined the energies and forces of the force field expressions, computed using the OpenMM software package,[98] and the neural network energies and forces, which are computed using PyTorch.[99] The simulations were also run at 300K with a Langevin integrator. A 0.005 fs^{-1} friction coefficient was used, and a 0.5 fs time step was used to integrate the nuclear equations of motion. The 0.5 fs time step is needed for good energy conservation with the anharmonic restraining potential used for the Drude oscillators (discussed in the Supporting Information).[100] These simulations were performed *in vacuo*, as were the AIMD simulations. A benchmark of the energy conservation of the PB/NN force field for a NVE simulation of the two-ion system is shown in the Supporting Information Figure S15.

Figure 6a and 6b show the free energy reaction profiles of the two ion system as computed from AIMD and the PB/NN force field respectively; for the two-ion PMF from the force field, we added an arbitrary shift of 3 kJ mol^{-1} in order to better compare its features to the AIMD result. Overall, there is good agreement between the free energy profiles, and the PB/NN force field predicts the reaction free energy with close to quantitative accuracy as compared to AIMD. Both PB/NN and AIMD predict a broad minimum basis for the $EMIM^+$/acetate reactants, and a barrierless transition state for the deprotonation reaction. There is no local minimum corresponding to the NHC/acetic acid products, and both PB/NN and AIMD predict that at 1.75 Å C–H distance, the NHC/acetic acid products are ∼ 8-10 kJ/mol higher in free energy than the reactants. There do exist small discrepancies between the PB/NN and AIMD free energy profiles, in terms of both the width of the reactant minimum along the C–H distance, and also the center of the reactant minimum; these discrepancies will be explained after first discussing the solvation effect.

Solvent effects on the reaction profile are analyzed by comparing predicted free energy surfaces of the "model solvent" four ion system, to corresponding profiles of the isolated reacting complex (two ion system). Free energy surfaces for the four ion, model solvent system are shown in Figures 6c and 6d as computed from AIMD and with the PB/NN force field respectively. Comparing Figures 6a)-d), several observations are made concerning the solvent effects on the reaction profile. First, the electrostatic interactions from the solvating ions broaden the minimum region associated with the reactant species ($EMIM^+$/acetate). This is seen by comparing e.g. Figure 6a) and Figure 6c), where the $EMIM^+$/acetate reactant minima (blue region) is signficantly broader when the reacting complex is solvated by the additional ions (four ion system, Figure 6c). Because the

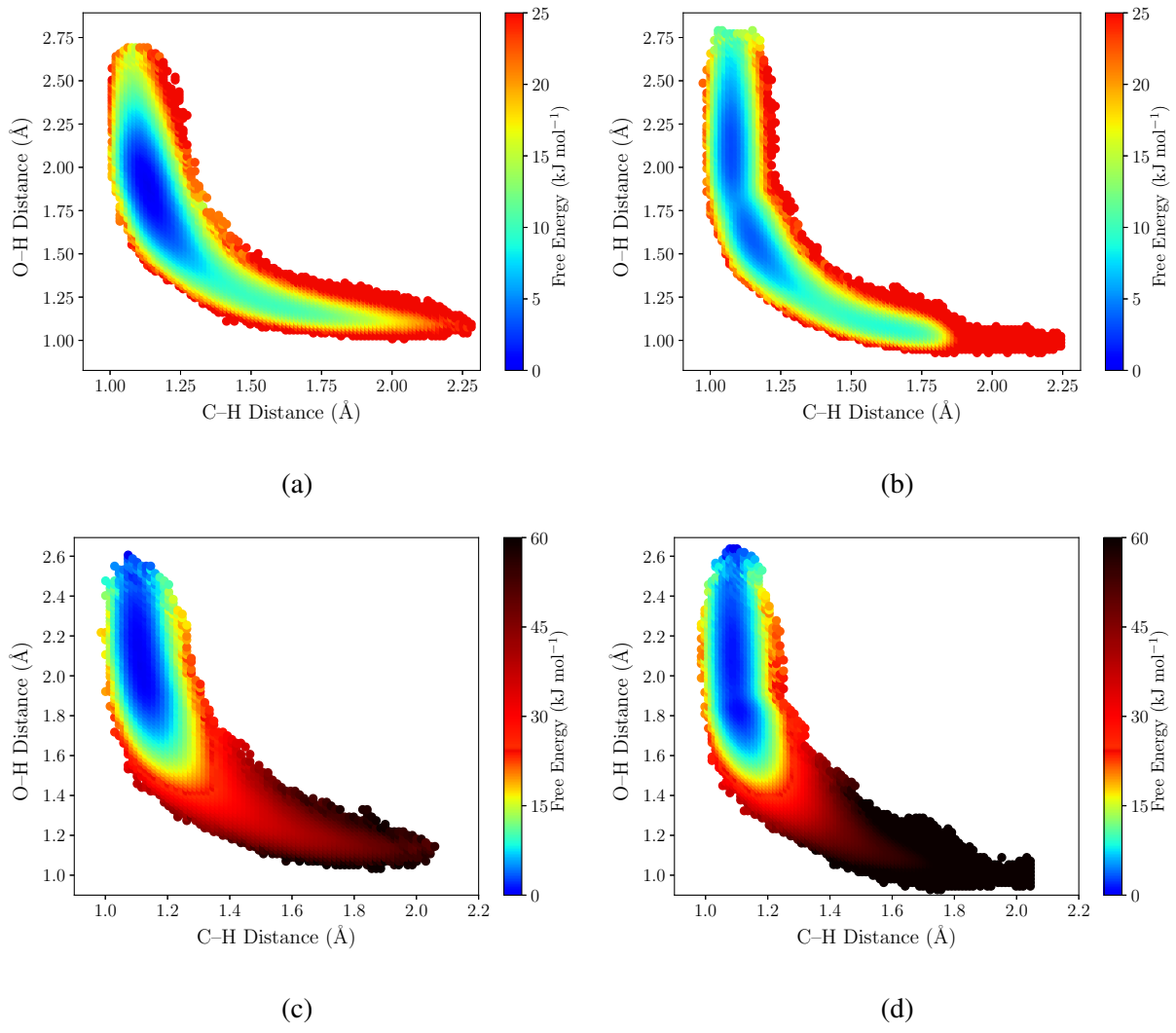

FIG. 6: Free energy surfaces for the EMIM$^+$/acetate deprotonation reaction with/without the "model" solvation environment. PMFs computed from AIMD simulations are shown in a) and c) for the two ion and four ion systems, respectively. PMFs computed from the PB/NN force field are shown in b) and d) for the two ion and four ion systems, respectively.

electrostatic interactions with "solvent" are much stronger for the EMIM$^+$/acetate ions in the "reactant" state compared to neutral NHC/acetic acid molecules in the product state, there is a substantial shift in the relative reactant/product free energies for the four ion compared to two ion systems. For example, the NHC/acetic acid products are $\sim$ 40-50 kJ mol^{-1} higher in free energy than EMIM$^+$/acetate reactions in presence of the two "solvating" ions, whereas the difference was only $\sim$ 10 kJ mol^{-1} for the isolated complex (note the difference in energy scales between Figures 6a,b and Figures 6c,d). This qualitative conclusion that carbene formation from EMIM$^+$/acetate

ions is destabilized in the presence of solvent, due to the large solvation energy of the reactants, is intuitive and is expected to be general to any condensed phase, chemical environment.

The PB/NN force field reproduces the solvation effect on the reaction profile in semi-quantiative agreement with the AIMD benchmarks. Note that exact quantitative agreement is not expected, for reasons discussed subsequently. The PB/NN force field predicts similar changes in the reaction profile with/without solvating ions (Figure 6b vs Figure 6d) relative to the AIMD benchmarks (Figure 6a vs Figure 6c). Although this benchmark is for a "model" solvation environment consisting of two additional solvating ions, the external electric field on the reacting complex is large and causes pronounced shifts of the reaction profile and resulting reactant/product relative free energies. We thus expect that the PB/NN force field should provide comparable accuracy for predicting solvation effects on the reaction profile in arbitrary condensed phase environments that exhibit strong electrostatic interactions. Such quantitative predictions would be important and necessary for evaluating the presence of trace, catalytic carbene species in imidazolium-based ionic liquids. Recall that similar to the EVB framework, the ansatz of the PB/NN force field construction is that solvent effects enter only through the diagonal Hamiltonian elements corresponding to the pure diabatic states (Section II C 3). Therefore, the accuracy of the PB/NN force field in capturing the solvent modulation of the reaction profile validates the diabatic decomposition of the force field, which was parameterized to symmetry adapted perturbation theory.

We finally discuss the subtle quantitative differences between free energy profiles predicted by the PB/NN force field (Figure 6b,d) and AIMD (Figure 6a,c). As always, there is the possibility that discrepancies are due to parameterization deficiencies; note, however, the very high accuracy of the energetic benchmarks of force field components in Figures 2, 3, and 4. A more likely source of discrepancy is the fundamental difference in electronic structure theory: *the level of theory between PB/NN and AIMD is consistent only in the transition state region, but not in the asymptotic region of dissociated reactants/products.* The PB/NN force field was trained to match (adiabatic) PBE-D3(BJ) energies/forces in the transition state region, but asymptotically matches SAPT description of intermolecular interactions in reactant/product regions. Even more subtle is that the $E_{Solute}^{Inter,NN}$ term is parameterized at SAPT0 level of theory, while force field interactions contributing to $E_{Solute,Solvent}^{Nonbonded,FF}$ were previously parameterized to DFT-SAPT (Section II C 3). Thus the asymptotic reactant and product states in the free energy profiles (Figures 6a-d) fundamentally differ in electronic structure description between the PB/NN and AIMD Hamiltonians. We believe this is the primary reason for why the solvent destabilization of the carbene products is predicted

to be more extreme by PB/NN compared to AIMD. The question of which prediction (PB/NN or AIMD) is more accurate requires consideration of the relative accuracy of PBE-D3(BJ) vs SAPT level of theory, which is beyond the scope of this work.

In future work, it may be profitable to explore other electronic structure choices for parameterizing the diabatic (Section II C 3) and coupling elements (Section II C 4) of the PB/NN potential. At the intersection of the pure diabat (reactant/product) and transition state region, the force field switches from SAPT0 to PBE-D3(BJ) parameterization. Due to differences in these electronic structure theories, there is no rigorous guarantee that the diabatic state will be strictly higher energy (or equal) compared to the underlying PBE-D3(BJ) adiabatic description (this would be rigorously true for equivalent levels of theory). Inspecting the free energy profile of the (two ion) reacting complex predicted by PB/NN (Figure 6b), slight error is observed in the center of the minimum (blue region) corresponding to the $EMIM^+$/acetate reactant at 1.2 Å C–H distance/1.8 Å O–H distance. This error is most likely due to the imperfect coupling of SAPT0/PBE-D3(BJ) descriptions as the force field transitions from the pure diabatic state. Alternative utilization of constrained DFT for diabatic parameterization would resolve this problem, but would likely sacrifice accuracy for asymptotic interactions for which SAPT is known to be very accurate.[93] It may be that a different flavor of SAPT, particularly DFT-SAPT, would lead to better coupling of the diabat/transition state region, and this will be explored in future work.

IV. CONCLUSION

We have described a new approach for developing physics-based/neural network (PB/NN) reactive force fields with the central goal of predicting solvent effects on reaction free energies with chemical accuracy. This approach follows an ansatz similar to the widely utilized EVB framework, but proposes novel combination of neural network and physics-based terms that follow a general *ab initio* parameterization approach. We have applied this methodology to study the deprotonation reaction between $EMIM^+$and acetate ions to form NHC and acetic acid, and analyze electric field modulation of the reaction free energy profile from a "model solvent" environment. Free energy profiles predicted by PB/NN are in good agreement with AIMD benchmarks, demonstrating that our PB/NN framework can accurately predict reaction free energy profiles in different chemical environments. In agreement with physical intuition, we show that the surrounding ionic environment significantly destabilizes carbene formation relative to the gas-phase, due to the large

solvation energies of the ionic reactant species. Our newly developed PB/NN force field should allow prediction of reaction free energies and equilibrium constants for carbene formation within various ionic liquid and solvent environments, to evaluate when and if trace amounts of these catalytic species are present.

While this work has focused on one specific reaction, our PB/NN approach is entirely general and can be applied to a wide variety of reactions. Additionally, as solvent interactions with the reacting complex are incorporated through physics-based force field terms, one can readily study the effects of a large number of different solvents for which force fields either already exist or can be constructed utilizing well-established methodology. This is the primary advantage of our PB/NN approach as compared to stand-alone neural network potentials, as solvent effects are not easily incorporated within neural network potentials in a general way. We have proposed the utilization of symmetry-adapted perturbation theory for parameterizing diabatic states of the PB/NN force field, as opposed to more traditionally utilized constrained DFT approaches. The advantage is that SAPT exhibits rigorous connection to intermolecular interaction terms of a force field and is highly accurate for describing non-covalent interactions. The disadvantage is the lack of rigorous connection between SAPT and the variational approach (DFT) used to parameterize the adiabatic reaction surface; however in this work, such introduced error is found to be small. It is possible that different flavors of SAPT, particularly DFT-SAPT may enhance accuracy and this will be explored in future work.

There are two aspects of our training data generation that will require greater attention when developing PB/NN force fields for more complex reactions. The first is adequately sampling the transition state region of the reaction surface; for the deprotonation reaction studied in this work, this was straightforward (direct AIMD) due to the lack of reaction barrier. However, reactions exhibiting significant barriers would require biased sampling approaches (with AIMD) to generate training data spanning the entire reaction coordinate, particularly in the transition state region. The second consideration is the total amount of training data required for full force field parameterization. Over one million quantum chemistry calculations were utilized for training, with the vast majority used for neural network parameterization. A more efficient approach would focus the training data by identifying the regions of configuration space where the neural networks exhibit the most uncertainty, using e.g. clustering or active learning approaches.[101–103] It is important to note however that this is a general issue for *any* neural network potential; in fact the issue is actually simplified for our PB/NN framework, as all of the employed neural networks are short-

range, and confined to minimal regions of phase space. We believe that restricting neural networks to small regions of phase space, and utilizing physics-based terms for asymptotic intermolecular interactions, is a robust approach for incorporating machine learning techniques within force field development.

SUPPLEMENTARY MATERIAL

See the supplementary material for the gas-phase potential energy surface of the reacting dimer compared to the PMF; a demonstration of intramolecular force field accuracy for the model carbene; further description of the E_{Solute}^{Morse} and $E_{Solute}^{Intra,NN}$ parameterization; $E_{Solute}^{Intra,NN}$ Fermi-Dirac function parameters; SchNet hyperparameters for training $E_{Solute}^{Intra,NN}$; a list of the $E_{Solute,Solvent}^{Nonbonded,FF}$ parameters and description of our parameter modifications; $E_{Solute}^{Inter,NN}$ Fermi-Dirac function parameters; a description of our process for obtaining configurations for training H_{12} from dataset 5; a description for how to obtain reference energies and forces for training H_{12} from the DFT energies in dataset 5; a table of the $E_{Solute}^{Intra,NN}$ MAE for energies and forces vs. the DFT reference data in datasets 1-4; a comparison of the accuracy of the $E_{Solute}^{Nonbonded,FF}$ compared to the SAPT0 reference data taken from both liquid MD and AIMD simulations; a description of how to obtain the polarization energy from the Drude oscillators in $E_{Solute,Solvent}^{Nonbonded,FF}$; a comparison of the $E_{Solute}^{Nonbonded,FF}$ energies vs. the SAPT0 energies in datasets 6 and 7; scans of the dissociating dimer with $E_{Solute}^{Inter,NN}$ with SchNet or AP-Net used as the neural network architecture; details about the C–H and O–H distances at which the umbrella potentials were centered; a table comparing the total PB/NN Hamiltonian energy and forces vs. the DFT energies and forces in dataset 5; a plot depicting the PB/NN vs. DFT energies for structures sampled from a AIMD simulation; and a plot demonstrating the energy conservation of the PB/NN force field for a NVE simulation.

ACKNOWLEDGMENTS

J.G.M. gratefully acknowledges financial support from the U.S. Department of Energy, Basic Energy Sciences, through Grant DE-SC0020279. Additional computational resources and services were provided by the Partnership for an Advanced Computing Environment (PACE) at Georgia Tech.

DATA AVAILABILITY STATEMENT

OpenMM force field files, produced neural network models and the ASE calculator used to run MD simulations of the PB/NN force field is available on GitHub at reference 97. The datasets used to construct the force field are available upon request.

REFERENCES

[1]C. J. Cramer and D. G. Truhlar, Chem. Rev. **99**, 2161 (1999).

[2]J. Tomasi, B. Mennucci, and R. Cammi, Chem. Rev. **105**, 2999 (2005).

[3]C. D. Snow, H. Nguyen, V. S. Pande, and M. Gruebele, Nature **420**, 102 (2002).

[4]J.-E. Shea and C. L. Brooks III, Annu. Rev. Phys. Chem. **52**, 499 (2001).

[5]W. Yang, Y. Q. Gao, Q. Cui, J. Ma, and M. Karplus, Proc. Natl. Acad. Sci. U.S.A. **100**, 874 (2003).

[6]J. W. Ponder and D. A. Case, Adv. Protein Chem. **66**, 27 (2003).

[7]F. Dommert, K. Wendler, R. Berger, L. Delle Site, and C. Holm, "Force fields for studying the structure and dynamics of ionic liquids: A critical review of recent developments," (2012).

[8]S. Cui, J. Liu, M. E. Selvan, D. J. Keffer, B. J. Edwards, and W. V. Steele, J. Phys. Chem. B **111**, 2208 (2007).

[9]G. Jindal and A. Warshel, J. Phys. Chem. B **120**, 9913 (2016).

[10]T. D. Kühne, M. Iannuzzi, M. Del Ben, V. V. Rybkin, P. Seewald, F. Stein, T. Laino, R. Z. Khaliullin, O. Schütt, F. Schiffmann, D. Golze, J. Wilhelm, S. Chulkov, M. H. Bani-Hashemian, V. Weber, U. Borštnik, M. Taillefumier, A. S. Jakobovits, A. Lazzaro, H. Pabst, T. Müller, R. Schade, M. Guidon, S. Andermatt, N. Holmberg, G. K. Schenter, A. Hehn, A. Bussy, F. Belleflamme, G. Tabacchi, A. Glöß, M. Lass, I. Bethune, C. J. Mundy, C. Plessl, M. Watkins, J. VandeVondele, M. Krack, and J. Hutter, J. Chem. Phys. **152**, 194103 (2020).

[11]Y. Han, D. Jiang, J. Zhang, W. Li, Z. Gan, and J. Gu, Front. Chem. Sci. Eng. **10**, 16 (2016).

[12]R. Slapikas, I. Dabo, and S. B. Sinnott, J. Chem. Phys. **152**, 224702 (2020).

[13]D. W. Brenner, O. A. Shenderova, J. A. Harrison, S. J. Stuart, B. Ni, and S. B. Sinnott, J. Phys. Condens. Matter **14**, 783 (2002).

[14]J. A. Harrison, J. D. Schall, S. Maskey, P. T. Mikulski, M. T. Knippenberg, and B. H. Morrow, "Review of force fields and intermolecular potentials used in atomistic computational materials

research," (2018).

[15]T. Liang, Y. K. Shin, Y.-T. Cheng, D. E. Yilmaz, K. G. Vishnu, O. Verners, C. Zou, S. R. Phillpot, S. B. Sinnott, and A. C. van Duin, Annu. Rev. Mater. Res. **43**, 109 (2013).

[16]A. C. Van Duin, A. Strachan, S. Stewman, Q. Zhang, X. Xu, and W. A. Goddard, J. Phys. Chem. A **107**, 3803 (2003).

[17]L. W. Bertels, L. B. Newcomb, M. Alaghemandi, J. R. Green, and M. Head-Gordon, J. Phys. Chem. A **124**, 5631 (2020).

[18]D. Furman and D. J. Wales, J. Phys. Chem. Letters , 7215 (2019).

[19]S. C. L. Kamerlin and A. Warshel, Wiley Interdiscip. Rev. Comput. Mol. Sci. **1**, 30 (2011).

[20]A. Warshel and R. M. Weiss, J. Am. Chem. Soc. **102**, 6218 (1980).

[21]J. Hwang, S. Creighton, G. King, D. Whitney, and A. Warshel, J. Chem. Phys. **89**, 859 (1998).

[22]G. Hong, E. Rosta, and A. Warshel, J. Phys. Chem. B **110**, 19570 (2006).

[23]M. Higashi and D. G. Truhlar, J. Chem. Theory Comput. **4**, 1032 (2008).

[24]S. C. Kamerlin and A. Warshel, Faraday Discuss. **145**, 71 (2010).

[25]J. Åqvist and A. Warshel, Chem. Rev. **93**, 2523 (1993).

[26]U. W. Schmitt and G. A. Voth, J. Phys. Chem. B **102** (1998), 10.1021/jp9818131.

[27]T. J. F. Day, A. V. Soudackov, M. Čuma, U. W. Schmitt, and G. A. Voth, J. Chem. Phys. **117**, 5839 (2002).

[28]Y. Wu, H. Chen, F. Wang, F. Paesani, and G. A. Voth, J. Phys. Chem. B **112**, 467 (2008).

[29]R. Biswas, Y.-L. S. Tse, A. Tokmakoff, and G. A. Voth, J. Phys. Chem. B **120**, 1793 (2016).

[30]G. A. Voth, Acc. Chem. Res. **39**, 143 (2006).

[31]M. Čuma, U. W. Schmitt, and G. A. Voth, J. Phys. Chem. A **105**, 2814 (2001).

[32]C. M. Maupin, K. F. Wong, A. V. Soudackov, S. Kim, and G. A. Voth, J. Phys. Chem. A **110**, 631 (2006).

[33]H. Chen, T. Yan, and G. A. Voth, J. Phys. Chem. A **113**, 4507 (2009).

[34]C. Knight, G. E. Lindberg, and G. A. Voth, J. Chem. Phys. **137** (2012), 10.1063/1.4743958.

[35]H. B. Schlegel and J. L. Sonnenberg, J. Chem. Theory Comput. **2**, 905 (2006).

[36]J. Behler, Angew. Chem. **56**, 12828 (2017).

[37]O. T. Unke and M. Meuwly, J. Chem. Theory Comput. **15**, 3678 (2019).

[38]L. Zhang, J. Han, H. Wang, R. Car, and E. Weinan, Phys. Rev. Lett. **120**, 143001 (2018).

[39]S. Amabilino, L. A. Bratholm, S. J. Bennie, A. C. Vaucher, M. Reiher, and D. R. Glowacki, J. Phys. Chem. A **123**, 4486 (2019).

[40]J. Behler, *Phys. Chem. Chem. Phys.*, **13**, 17930 (2011).

[41]H. Schreiber and O. Steinhauser, Chem. Phys. **168**, 75 (1992).

[42]G. S. Del Buono, F. E. Figueirido, and R. M. Levy, Chem. Phys. Lett. **263**, 521 (1996).

[43]L. Perera, U. Essmann, and M. L. Berkowitz, J. Chem. Phys. **102**, 450 (1995).

[44]B. Parsaeifard, D. S. De, J. A. Finkler, and S. Goedecker, Condens. Matter **6**, 9 (2021).

[45]D. P. Metcalf, A. Jiang, S. A. Spronk, D. L. Cheney, and C. D. Sherrill, J. Chem. Inf. Model. **61**, 115 (2021).

[46]Z. L. Glick, A. Koutsoukas, D. L. Cheney, and C. D. Sherrill, J. Chem. Phys. **154**, 224103 (2021).

[47]D. M. Flanigan, F. Romanov-Michailidis, N. A. White, and T. Rovis, Chem. Rev. **115**, 9307 (2015).

[48]M. N. Hopkinson, C. Richter, M. Schedler, and F. Glorius, Nature **510**, 485 (2014).

[49]R. Ratti, Adv. Chem. **2014**, 1 (2014).

[50]I. Chiarotto, L. Mattiello, F. Pandolfi, D. Rocco, and M. Feroci, Front. Chem. **6**, 355 (2018).

[51]I. Chiarotto, M. Feroci, G. Forte, M. Orsini, and A. Inesi, ChemElectroChem **1**, 1525 (2014).

[52]M. Feroci, I. Chiarotto, and A. Inesi, Catalysts **6**, 178 (2016).

[53]M. Thomas, M. Brehm, O. Hollóczki, and B. Kirchner, Chem. Eur. J. **20**, 1622 (2014).

[54]N. M. A. N. Daud, E. Bakis, J. P. Hallett, C. C. Weber, and T. Welton, Chem. Commun. **53**, 11154 (2017).

[55]S. Gehrke, W. Reckien, I. Palazzo, T. Welton, and O. Hollóczki, Eur. J. Org. Chem. **2019**, 504 (2019).

[56]Z. Kelemen, O. Hollóczki, J. Nagy, and L. Nyulászi, Org. Biomol. Chem. **9**, 5362 (2011).

[57]A. C. Baumruck, D. Tietze, A. Stark, and A. A. Tietze, J. Org. Chem. **82**, 7538 (2017).

[58]F. Pandolfi, M. Feroci, and I. Chiarotto, ChemistrySelect **3**, 4745 (2018).

[59]I. Chiarotto, M. Feroci, G. Forte, and A. Inesi, Electrochim. Acta **176**, 627 (2015).

[60]I. Chiarotto, M. Feroci, and A. Inesi, New J. Chem. **41**, 7840 (2017).

[61]P. Jain, V. R. Chaudhari, and A. Kumar, Phys. Chem. Chem. Phys. **21**, 24126 (2019).

[62]J. F. Wishart, Energy Environ. Sci. **2**, 956 (2009).

[63]S. Schneider, T. Hawkins, M. Rosander, G. Vaghjiani, S. Chambreau, and G. Drake, Energy Fuels **22**, 2871 (2008).

[64]S. D. Chambreau, A. C. Schenk, A. J. Sheppard, G. R. Yandek, G. L. Vaghjiani, J. Maciejewski, C. J. Koh, A. Golan, and S. R. Leone, J. Phys. Chem. A **118**, 11119 (2014).

[65]N. Artrith, T. Morawietz, and J. Behler, Physical Review B **83**, 153101 (2011).

[66]J. B. Schriber, D. R. Nascimento, A. Koutsoukas, S. A. Spronk, D. L. Cheney, and C. D. Sherrill, J. Chem. Phys. **154**, 184110 (2021).

[67]T. Bereau, R. A. DiStasioJr., A. Tkatchenko, and O. A. v. Lilienfeld, J. Chem. Phys. **148**, 241706 (2018).

[68]B. Hartke and S. Grimme, Phys. Chem. Chem. Phys. **17**, 16715 (2015).

[69]J. L. Sonnenberg and H. B. Schlegel, Mol. Phys. **105**, 2719 (2007).

[70]Y. T. Chang and W. H. Miller, J. Phys. Chem. **94**, 5884 (1990).

[71]J. P. Perdew, K. Burke, and M. Ernzerhof, Phys. Rev. Lett. **77**, 3865 (1996).

[72]S. Grimme, J. Antony, S. Ehrlich, and H. Krieg, J. Chem. Phys. **132**, 154104 (2010).

[73]S. Grimme, S. Ehrlich, and L. Goerigk, J. Comput. Chem. **32**, 1456 (2011).

[74]S. Goedecker and M. Teter, Phys. Rev. B **54**, 1703 (1996).

[75]P. Pulay, Chem. Phys. Lett. **73**, 393 (1980).

[76]D. G. Smith, L. A. Burns, A. C. Simmonett, R. M. Parrish, M. C. Schieber, R. Galvelis, P. Kraus, H. Kruse, R. Di Remigio, A. Alenaizan, A. M. James, S. Lehtola, J. P. Misiewicz, M. Scheurer, R. A. Shaw, J. B. Schriber, Y. Xie, Z. L. Glick, D. A. Sirianni, J. S. O'Brien, J. M. Waldrop, A. Kumar, E. G. Hohenstein, B. P. Pritchard, B. R. Brooks, H. F. Schaefer, A. Y. Sokolov, K. Patkowski, A. E. DePrince, U. Bozkaya, R. A. King, F. A. Evangelista, J. M. Turney, T. D. Crawford, and C. D. Sherrill, J. Chem. Phys. **152**, 184108 (2020).

[77]R. Salomon-Ferrer, D. A. Case, and R. C. Walker, Wiley Interdiscip. Rev. Comput. Mol. Sci. **3**, 198 (2013).

[78]B. R. Brooks, C. L. Brooks, A. D. Mackerell, L. Nilsson, R. J. Petrella, B. Roux, Y. Won, G. Archontis, C. Bartels, S. Boresch, A. Caflisch, L. Caves, Q. Cui, A. R. Dinner, M. Feig, S. Fischer, J. Gao, M. Hodoscek, W. Im, K. Kuczera, T. Lazaridis, J. Ma, V. Ovchinnikov, E. Paci, R. W. Pastor, C. B. Post, J. Z. Pu, M. Schaefer, B. Tidor, R. M. Venable, H. L. Woodcock, X. Wu, W. Yang, D. M. York, and M. Karplus, J. Comput. Chem. **30**, 1545 (2009).

[79]Lindahl, Abraham, Hess, and v. d. Spoel, *GROMACS 2021 Manual* (2021).

[80]J. G. McDaniel, E. Choi, C. Y. Son, J. R. Schmidt, and A. Yethiraj, J. Phys. Chem. B **120**, 7024 (2016).

[81]Z. Liu, S. Huang, and W. Wang, J. Phys. Chem. B **108**, 12978 (2004).

[82]K. Schütt, P.-J. Kindermans, H. E. S. Felix, S. Chmiela, A. Tkatchenko, and K.-R. Müller, "SchNet: A continuous-filter convolutional neural network for modeling quantum interactions,"

(2017).

[83]J. G. McDaniel and J. R. Schmidt, Annu. Rev. Phys. Chem **67**, 467 (2016).

[84]J. G. McDaniel and J. R. Schmidt, J. Phys. Chem. A **117**, 2053 (2013).

[85]E. Choi, J. G. McDaniel, J. R. Schmidt, and A. Yethiraj, J. Phys. Chem. Lett. **5**, 2670 (2014).

[86]J. G. McDaniel and A. Yethiraj, J. Phys. Chem. Lett. **9**, 4765 (2018).

[87]J. A. Lemkul, J. Huang, B. Roux, and J. Alexander D. MacKerell, Chem. Rev. **116**, 4983 (2016).

[88]J. Huang, J. A. Lemkul, P. K. Eastman, and A. D. MacKerell, J. Comput. Chem. **39**, 1682 (2018).

[89]M. J. V. Vleet, A. J. Misquitta, A. J. Stone, and J. R. Schmidt, J. Chem. Theory Comput. **12**, 3851 (2016).

[90]K. Patkowski, Wiley Interdiscip. Rev. Comput. Mol. Sci. **10** (2020), 10.1002/wcms.1452.

[91]B. Kaduk, T. Kowalczyk, and T. Van Voorhis, Chem. Rev. **112**, 321 (2012).

[92]W. D. Derricotte, J. Phys. Chem. A **123**, 7881 (2019).

[93]T. M. Parker, L. A. Burns, R. M. Parrish, A. G. Ryno, and C. D. Sherrill, J. Chem. Phys. **140**, (2014).

[94]Z. L. Glick, D. P. Metcalf, A. Koutsoukas, S. A. Spronk, D. L. Cheney, and C. D. Sherrill, J. Chem. Phys. **153**, 044112 (2020).

[95]S. Kumar, J. M. Rosenberg, D. Bouzida, R. H. Swendsen, and P. A. Kollman, J. Comput. Chem. **16**, 1339 (1995).

[96]A. Hjorth Larsen, J. Jørgen Mortensen, J. Blomqvist, I. E. Castelli, R. Christensen, M. Dułak, J. Friis, M. N. Groves, B. Hammer, C. Hargus, E. D. Hermes, P. C. Jennings, P. Bjerre Jensen, J. Kermode, J. R. Kitchin, E. Leonhard Kolsbjerg, J. Kubal, K. Kaasbjerg, S. Lysgaard, J. Bergmann Maronsson, T. Maxson, T. Olsen, L. Pastewka, A. Peterson, C. Rostgaard, J. Schiøtz, O. Schütt, M. Strange, K. S. Thygesen, T. Vegge, L. Vilhelmsen, M. Walter, Z. Zeng, and K. W. Jacobsen, J. Phys. Condens. Matter. **29**, 273002 (2017).

[97]J. Stoppelman, "Ase-pbnn-calculator," (2021), `https://github.com/jstoppelman/ASE-PBNN-Calculator`.

[98]P. Eastman, J. Swails, J. D. Chodera, R. T. McGibbon, Y. Zhao, K. A. Beauchamp, L. P. Wang, A. C. Simmonett, M. P. Harrigan, C. D. Stern, R. P. Wiewiora, B. R. Brooks, and V. S. Pande, PLOS Comput. Biol. **13**, e1005659 (2017).

[99]A. Paszke, S. Gross, F. Massa, A. Lerer, J. Bradbury, G. Chanan, T. Killeen, Z. Lin, N. Gimelshein, L. Antiga, A. Desmaison, A. Kopf, E. Yang, Z. DeVito, M. Raison, A. Tejani, S. Chilamkurthy, B. Steiner, L. Fang, J. Bai, and S. Chintala, in *Advances in Neural Information Processing Systems 32* (Curran Associates, Inc., 2019) pp. 8024–8035.

[100]Y. Luo, W. Jiang, H. Yu, A. D. MacKerell, and B. Roux, Faraday Discuss. **160**, 135 (2013).

[101]R. Jinnouchi, K. Miwa, F. Karsai, G. Kresse, and R. Asahi, J. Phys. Chem. Lett. **11**, 6946 (2020).

[102]R. K. Lindsey, L. E. Fried, N. Goldman, and S. Bastea, J. Chem. Phys. **153**, 134117 (2020).

[103]G. Fonseca, I. Poltavsky, V. Vassilev-Galindo, and A. Tkatchenko, J. Chem. Phys. **154**, 124102 (2021).